Inorganic Chemistry

Article

pubs.acs.org/IC

Computational Chemistry Meets Experiments for Explaining the Geometry, Electronic Structure, and Optical Properties of $Ca_{10}V_6O_{25}$

Mayara Mondego Teixeira,[*,†] Regiane Cristina de Oliveira,[†] Marisa Carvalho Oliveira,[†,‡] Renan Augusto Pontes Ribeiro,[§] Sergio R. de Lazaro,[§] Máximo Siu Li,[∥] Adenilson J. Chiquito,[⊥] Lourdes Gracia,[#] Juan Andrés,[‡] and Elson Longo[†]

[†]CDMF-UFSCar, Universidade Federal de São Carlos, P.O. Box 676, 13565-905 São Carlos, SP Brazil

[‡]Departamento de Química Física i Analítica, Universitat Jaume I, 12071, Castelló de la Plana, Spain

[§]Departamento de Química, Universidade Estadual de Ponta GrosCsa, Av. General Carlos Cavalcanti, 4748, 84030-900, Ponta Grossa, PR, Brazil

[∥]IFSC-Universidade de São Paulo, P.O. Box 369, 13560-970, São Carlos, São Paulo, Brazil

[⊥]Departamento de Física, Universidade Federal de São Carlos, Rod. Washington Luiz, km 235, CP 676, CEP 13565-905, São Carlos, SP, Brazil

[#]Departamento de Química Física, Universitat de València, 46100 Burjassot, Spain

Supporting Information

ABSTRACT: In this paper, we present a combined experimental and theoretical study to disclose, for the first time, the structural, electronic, and optical properties of $Ca_{10}V_6O_{25}$ crystals. The microwave-assisted hydrothermal (MAH) method has been employed to synthesize these crystals with different morphologies, within a short reaction time at 120 °C. First-principle quantum mechanical calculations have been performed at the density functional theory level to obtain the geometry and electronic properties of $Ca_{10}V_6O_{25}$ crystal in the fundamental and excited electronic states (singlet and triplet). These results, combined with the measurements of X-ray diffraction (XRD) and Rietveld refinements, confirm that the building blocks lattice of the $Ca_{10}V_6O_{25}$ crystals consist of three types of distorted 6-fold coordination $[CaO_6]$ clusters: octahedral, prism and pentagonal pyramidal, and distorted tetrahedral $[VO_4]$ clusters. Theoretical and experimental results on the structure and vibrational frequencies are in agreement. Thus, it was possible to assign the Raman modes for the $Ca_{10}V_6O_{25}$ superstructure, which will allow us to show the structure of the unit cell of the material, as well as the coordination of the Ca and V atoms. This also allowed us to understand the charge transfer process that happens in the singlet state (s) and the excited states, singlet (s*) and triplet (t*), generating the photoluminescence emissions of the $Ca_{10}V_6O_{25}$ crystals.

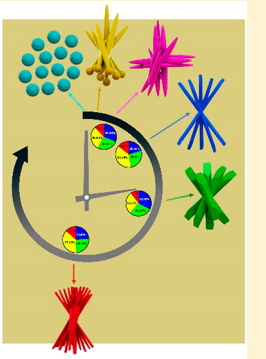

1. INTRODUCTION

The members of the calcium vanadate family, such as $Ca_{0.5}V_3O_8$,[1] CaV_4O_9, CaV_3O_7 and CaV_2O_5,[2] CaV_2O_6,[3] $CaVO_3$,[4] CaV_6O_{16},[5] $Ca_2V_2O_7$,[6] $Ca_3V_2O_8$,[7] $Ca_4V_4O_{14}$,[8] $Ca_7V_4O_{17}$,[9] and $Ca_{10}V_6O_{25}$[5,10,11] have attracted increasing interest, because of their structure, compositional diversity, and physical and chemical properties, which facilitate a wide range of technological applications in the fields of magnetism, electrochemistry, catalysis, and optical devices.[1,2,10−16]

In particular, $Ca_{10}V_6O_{25}$ has drawn attention, because of its geometric structure, in which both Ca and V cations adopt different local coordinations,[5,10] with a promising potential in electronic, biomedical, and semiconductor applications.[10,17] Moreover, Pei et al.[11] observed that the $Ca_{10}V_6O_{25}$ nanorod modified glassy carbon electrode, which presents good performance in the electrochemical detection of tartaric acid, is promising for the development of electrochemical sensors for tartaric acid: However, information about its structure and related materials is scarce and incomplete.[5,10,11,13,17,18] For related compounds, Adams and Gardner[19] analyze the single-crystal vibrational spectra of apatite ($Ca_5(PO_4)_3F$), vanadinite ($Pb_5(VO_4)_3Cl$), and mimetite ($Pb_5(AsO_4)_3Cl$). Petit et al.[20] synthesized $Ca_{10}(PO_4)_{6-x}(VO_4)_x(OH)_2$ (where $0 \le x \le 6$) and studied the vibrational modes in related materials. Frost et al.[21] assigned the vibrational modes to vanadinite $[Pb_5(VO_4)_3Cl]$; meanwhile, Bartholomai and Klee[22] resolved the vibrational modes for the apatites pyromorphite $[Pb_5(PO_4)_3Cl]$, vanadinite $[Pb_5(VO_4)_3Cl]$, and mimetite $[Pb_5(AsO_4)_3Cl]$.

For the synthesis of $Ca_{10}V_6O_{25}$ crystals, different authors reported the use of precipitation and hydrothermal methods to obtain crystals with diverse morphologies.[5,10,11] In particular, Hojamberdiev et al.[10] synthesized $Ca_{10}V_6O_{25}$ via hydrothermal processing in a basic medium under the pH range of 12.0−13.5, the temperature range of 120−180 °C, and reaction times of 12, 24, and 48 h. These authors concluded that the above reaction

Received: October 2, 2018

DOI: 10.1021/acs.inorgchem.8b02807
Inorg. Chem. XXXX, XXX, XXX−XXX

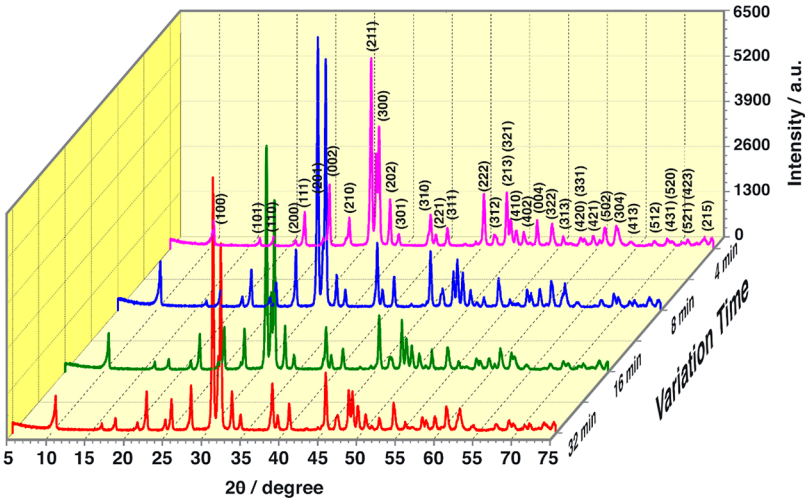

Figure 1. XRD patterns and the Miller indices in accordance with JCPDS File No. 52-649 for the $Ca_{10}V_6O_{25}$ processed at 120 °C, as a function of synthesis time.

parameters have a strong influence on the morphology of the as-synthesized $Ca_{10}V_6O_{25}$ crystals, and they obtained various morphologies, such as rods and spherical, ricelike, and bundled particles. However, these methods require high temperatures, long processing times (from a few hours to a few days), and expensive equipment. However, the use of microwaves has improved the synthesis procedure since materials were obtained at shorter times and lower temperatures. Moreover, there is increased interest in developing the microwave-assisted hydrothermal (MAH) method, because it has advantages of being a faster, simpler, and more efficient route to obtain single-phase crystals with good reproducibility.[23−26] In this context, by using the MAH method, our group could synthesize various metal oxides, such as $BaZrO_3$,[27] CuO with catalytic activity,[28] $SrTiO_3$ with photocatalytic activity,[29] and α-Ag_2WO_4 as acetone gas sensors.[30]

The present paper reports the synthesis of monophasic $Ca_{10}V_6O_{25}$ crystals by using the MAH method at a temperature of 120 °C within a short synthesis time. The geometry, electronic structure, optical properties, and morphology of the crystals were examined using X-ray diffraction (XRD) patterns with Rietveld refinement, Raman spectroscopy, ultraviolet−visible (UV-vis) diffuse reflectance spectroscopy (DRS), photoluminescence (PL) measurements, transmission electron microscopy (TEM), energy-dispersive X-ray spectroscopy (EDS), field-emission scanning electron microscopy (FE-SEM), and current−voltage measurements. First-principles calculations at the density functional theory (DFT) level were performed to complement the experimental results, in order to elucidate the geometry, electronic structure, and optical properties of $Ca_{10}V_6O_{25}$ crystals. The localization and characterization of the excited singlet and triplet electronic states allows us to rationalize the PL emissions of this material, which are reported for first time in the present work.

2. EXPERIMENTAL PROCEDURE

2.1. Synthesis. The synthesis of the $Ca_{10}V_6O_{25}$ crystals follows the procedure proposed by Hojamberdiev et al.:[10] 2 mmol of NH_4VO_3 (≥99.9%, Sigma−Aldrich) was dissolved in 25 mL of distilled water, and heated thereafter at 50 °C under magnetic stirring until the reagent was dissolved completely. Separately, 1.6 mmol of $CaCl_2{\cdot}2H_2O$ (99.0%−105.0%, synth) was dissolved in 25 mL of distilled water at room temperature. After complete dissolution of the reactants, the solutions were mixed at room temperature and the pH of the solution was adjusted to 12.5 via the dropwise addition of a 6 mol/L KOH aqueous solution. The final volume was adjusted to 70 mL. Subsequently, the solution was stirred for 10 min and thereafter, it was transferred to the MAH system at the temperature of 120 °C and maintained for different time durations of 4, 8, 16, and 32 min. The precipitates formed were collected at room temperature, washed with distilled water until the pH was neutralized, and dried in a conventional furnace at 60 °C for 12 h. The samples obtained after the different time durations were denoted as CaVO-4, CaVO-8, CaVO-16, and CaVO-32, corresponding to the synthesis times of 4, 8, 16, and 32 min, respectively.

2.2. Characterizations. $Ca_{10}V_6O_{25}$ samples were characterized by X-ray diffraction (XRD) using a diffractometer (Model DMax/2500PC, Rigaku, Japan), with Cu Kα radiation (λ = 1.5406 Å) in the 2θ range of 5°−75° with a scanning rate of 0.02°/min. The Rietveld refinements using the general structure analysis (GSAS) program, the scan rate of 0.01°/min for 2θ range of 5°−110°. Raman spectroscopy measurements were performed using a spectrometer (Model T64000, Horiba Jobin-Yvon, Japan) coupled to a CCD Synapse detector and an argon-ion laser, operating at 514 nm with a maximum power of 7 mW. The spectra were measured in the wavenumber range of 25−1200 cm^{-1}. Ultraviolet−visible (UV-vis) spectra were obtained using a spectrophotometer (Model Cary 5G, Varian, USA) in diffuse reflection mode. The morphologies of the samples were examined using field-emission scanning electron microscopy (FE-SEM) (Supra 35-VP Carl Zeiss, Germany) operated at 15 kV. PL measurements were performed with a Monospec 27 monochromator (Thermal Jarrel Ash, USA) coupled with a R955 photomultiplier (Hamamatsu Photonics, Japan). A krypton ion laser (Coherent Innova 200 K, USA; λ = 350 nm) was used as the excitation source with an incident power of ~14 mW on the samples. All measurements were performed at room temperature. For the Raman, PL, and UV-vis characterizations: the $Ca_{10}V_6O_{25}$ samples, in the powder form, were placed in the respective port samples of each piece of equipment.

For the current−voltage (I−V) characterizations, 6-mm-diameter pressed pellets were made and the measurements were performed at room temperature, using silver electrical contacts 75 nm thick, which were obtained on an evaporator (Model AUTO 306, Edwards) under a pressure of 10^{-7} mbar. The current was determined by a Keithley 6517B electrometer coupled to a probing positioning system.

3. COMPUTATIONAL METHODS

Calculations were performed using the periodic ab initio CRYSTAL14 package,[31] based on density functional theory (DFT) using hybrid functional of a nonlocal exchange

DOI: 10.1021/acs.inorgchem.8b02807
Inorg. Chem. XXXX, XXX, XXX−XXX

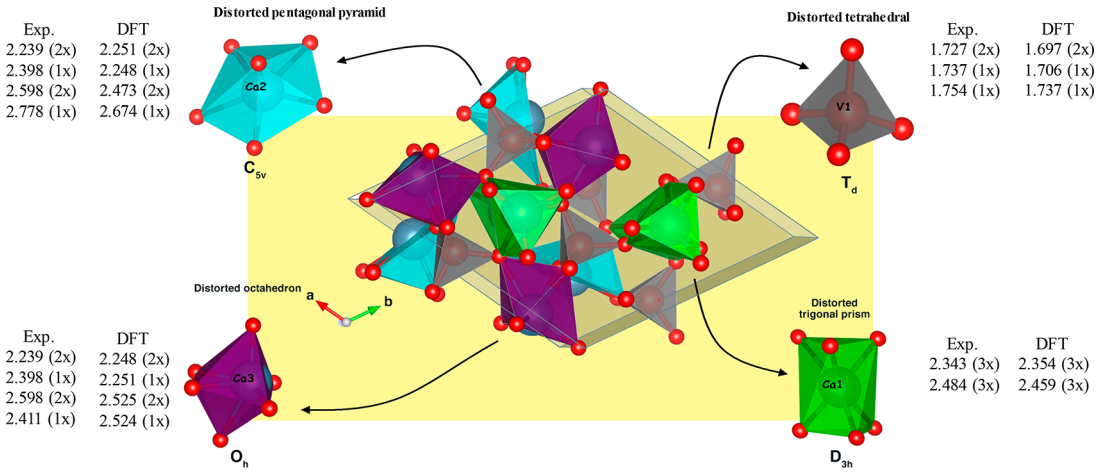

Figure 2. Schematic representation of the hexagonal unit cells of $Ca_{10}V_6O_{25}$ showing the local structures for $[CaO_6]$ and $[VO_4]$ clusters (in gray) and the bond lengths (in Å) obtained from Rietveld refinement and DFT calculations. Green, cyan, and purple polyhedrons represent the prismatic, pentagonal-pyramid, and octahedral symmetries associated with $[CaO_6]$ clusters, respectively. The values 1x, 2x, and 3x correspond to the bond multiplicity.

functional developed from Becke, combined with a correlation functional based on the gradient of electronic density developed from Lee, Yang, and Parr (B3LYP).[32,33] This computational technique has been successful for the study of the electronic and structural properties of various materials, including vanadates and several other oxides.[34−38] The Ca, V, and O atoms were described by standard atom-centered all-electron basis sets: 86-511d3G, 86-411d4G, and 6-31d1G, respectively.[39−41]

Full optimization of the $Ca_{10}V_6O_{25}$ structure was performed. The initial geometry was obtained from XRD experimental results, considering the removal of one O atom in this system through the ATOMREMO option provided by the CRYSTAL program. The convergence criteria for both monoelectronic and bielectronic integrals was set as 10^{-8} Hartree. Regarding the density matrix diagonalization, the reciprocal space net was described by a shrinking factor set to 4, corresponding to 12 *k*-points within the irreducible part of the Brillouin zone in accordance with the Monkhorst−Pack method.[42] In order to understand the PL mechanism associated with $Ca_{10}V_6O_{25}$ material, both excited singlet states (s*) and excited triplet states (t*) have been localized and characterized, following the previous strategies developed by our group.[43−48] For the s* model, we consider an off-center V displacement of 0.1 Å in the *z*-direction. In this case, the t* model state was reproduced fixing the difference between spin-up (α) and spin-down (β) ($n\alpha - n\beta = 2$) along the self-consistent field (SCF) calculations. The electronic structure was investigated from band structure and density of states (DOS).

4. RESULTS AND DISCUSSION

4.1. XRD and Rietveld Refinements. Figure 1 and Figure S1 (in the Supporting Information) present the XRD patterns and Rietveld refinement plot of the 3D $Ca_{10}V_6O_{25}$ crystals, respectively. The XRD patterns in Figure 1 show that all of the samples exhibit well-defined peaks suggesting an ordered long-range arrangement in the crystal lattice, for the samples obtained at 120 °C via MAH. The Miller indices of the peaks are in accordance with Joint Committee on Powder Diffraction Standards (JCPDS) No. 52-649 for the $Ca_{10}V_6O_{25}$ phase with a hexagonal structure and the space group of $P6_3/m$, indicating the absence of additional phases. Thus, the efficient internal heating by direct coupling of microwave energy with the molecules was efficient in obtaining the pure $Ca_{10}V_6O_{25}$ phase at a temperature of 120 °C within short reaction times in the MAH method. The Rietveld refinement method was applied to confirm the three-dimensional (3D) structure of $Ca_{10}V_6O_{25}$. The refinement was performed using the GSAS program.[49,50]

No Inorganic Crystal Structure Database (ICSD) card related to this structure has been reported in the literature. ICSD No. 24100, for calcium tris(tetraoxochromate(V)) hydroxide, reported by Wilhelmi et al., has been used, because it has a similar crystallographic structure.[51] The obtained results are displayed in Table S1 in the Supporting Information. The experimentally observed XRD patterns and the theoretically calculated data exhibit small differences near zero on the intensity scale, as illustrated by the line $Y_{Obs}-Y_{Calc}$; moreover, the fitting parameters (R_{Bragg} and χ^2) indicate consistency between the calculated data and observed XRD patterns for the $Ca_{10}V_6O_{25}$ microcrystals obtained at 120 °C. The smaller values of fitting parameters obtained for the CaVO-4 and CaVO-16 samples indicate greater network symmetry and long-range ordering than those of the powders of CaVO-8 and CaVO-32. Table S1 shows that the CaVO-4 and CaVO-16 samples present a smaller cell volume, associated with the volume contraction at the unit cell. The lattice parameters (*a*, *b*, and *c*) and bond angle (β) estimated from the refinement confirm the hexagonal structure.

Figure 2 displays a schematic representation of a hexagonal unit cell of the $Ca_{10}V_6O_{25}$ crystal, modeled from the Rietveld refinement data and optimized with DFT/B3LYP level of theory, in which the symmetry and geometry of the local coordination of Ca and V cations forming the building blocks of this crystal are depicted.

The unit cell shown in Figure 2 was modeled using the visualization system for electronic and structural analysis (VESTA) program (version 3.4.0) for Windows 7−64-bit0.[52,53] An analysis of the results indicates that the V cations are coordinated with four oxygen anions to form distorted tetragonal $[VO_4]_d$ clusters, whereas the Ca cations exhibit three types of octahedral $[CaO_6]_d$ clusters with highly distorted geometries. The Ca1, Ca2, Ca3, and Ca4 cations form distorted trigonal prisms, the Ca5, Ca7, and Ca8 cations form distorted octahedra, and the Ca6, Ca9, and Ca10 cations form distorted

DOI: 10.1021/acs.inorgchem.8b02807
Inorg. Chem. XXXX, XXX, XXX−XXX

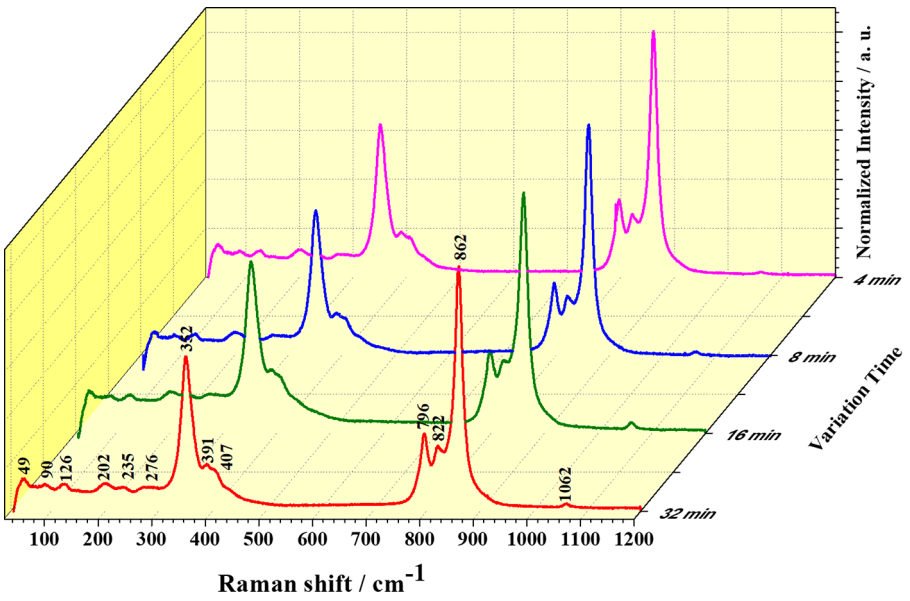

Figure 3. Raman spectra in the wavenumber range of 25−1200 cm^{-1} of the $Ca_{10}V_6O_{25}$ crystals processed at 120 °C, as a function of synthesis time.

pentagonal pyramids. Furthermore, it was observed that the theoretical values are consistent with the experimental results. This large variety of V−O and Ca−O bonds and O−V−O and O−Ca−O bond angles is responsible for the order/disorder effects, which are associated with the different degrees of distortion and the wide range of bonding patterns of these clusters. The structural distortions within the $[CaO_6]_d$ and $[VO_4]_d$ clusters then generate a polarization in the crystal structure, because of the displacement of Ca and V cations.

4.2. Raman Spectra. The $Ca_{10}V_6O_{25}$ crystal exhibits a hexagonal structure with the space group $P6_3/m$ (C_{6h}^2) and the following vibrational modes:

$$\Gamma = 1A_u + 2E_{1u} + 2B_u + 1E_{2u} + 2A_g + E_{1g} + 2B_g + 3E_{2g}$$

For a perfect and orderly crystalline structure with this space and point group symmetry, six active Raman modes are expected as follows:

$$\Gamma = 2A_g + E_{1g} + 3E_{2g}$$

In this study, first-principles calculations predict 123 active Raman and infrared modes for the $Ca_{10}V_6O_{25}$ structure, of which 63 Raman modes match the following decomposition at the Γ point: ($\Gamma = 24A_g' + 24E_g' + 15E_g''$). The experimental vibrational Raman frequencies were obtained in the wavenumber range of 25−1200 cm^{-1}, and all the samples exhibited 13 experimental modes, as shown in Figure 3. However, some of them are not observed experimentally, because of either overlapping bands or low intensity.

At lower frequencies, the peaks obtained through B3LYP calculations at 89.38 cm^{-1} (exp 90 cm^{-1}), 124.14 cm^{-1} (exp 126 cm^{-1}), 204.69 cm^{-1} (exp 202 cm^{-1}), 237 cm^{-1} (exp 235 cm^{-1}), and 262.58 cm^{-1} (exp 276 cm^{-1}) are associated with the lattice modes of $[CaO_6]$ clusters.[19] The intense band at 348.26 cm^{-1} (exp 352 cm^{-1}) is associated with the A_g mode of bending vibration of the O−V−O bond of ν_3. The peaks at 379.40 cm^{-1} (exp 391 cm^{-1}) and 400.22 cm^{-1} (exp 407 cm^{-1}) are assigned to the A_g bending vibration of the O−V−O bond of ν_4. The other band at 796 cm^{-1} is related to the E_{2g} antisymmetric stretching of the VO_4 of ν_3. Moreover, the peaks located at 859.60 cm^{-1} (exp 822 cm^{-1}) and the most intense band at 867.34 cm^{-1} (exp 862 cm^{-1}) may be attributed to the A_g symmetrical stretching vibration of the V−O bond of ν_1.[20−22] The band located at 1020.96 cm^{-1} (exp 1062 cm^{-1}) corresponds to the internal modes assigned to the symmetric stretching vibrations of the $[VO_4]$ cluster.

As reported in the literature,[54,55] a solid with the local structural order has a sharp, intense, and well-defined vibrational bands. We have compared the full width at half-maximum (fwhm) of the peak of 352 cm^{-1} in the Raman spectra of all the samples (Figure S2 in the Supporting Information). Analysis of these phonon line widths reveals similar structural disorder at the $[VO_4]$ cluster.

Table S2 shows the calculated B3LYP frequencies (ω) of the Raman active modes at the Γ point for the $P6_3/m$ structure. The results of the B3LYP calculation present an acoustic mode of zero frequency. with É symmetry, and an imaginary frequency (−55.02 cm^{-1}), which reveals that the $Ca_{10}V_6O_{25}$ structure optimized in the $P6_3/m$ space group has a structural instability at Γ and corresponds to a saddle point on a very flat potential energy surface after removing an oxygen atom in the initial structure. Various numerical checks (e.g., setting a better energy convergence, strengthening of the optimization criteria, decreasing the symmetry constraints) have been performed to ensure that the negative frequency was not an artifact of the calculations.

4.3. Morphology and Growth Mechanism. Variation in the synthesis time (4, 8, 16, and 32 min) influences the morphology of the $Ca_{10}V_6O_{25}$ crystals (see Figure 4).

The growth process can be monitored at different times, maintaining the temperature constant at 120 °C. At 4 min, after the formation of the first nanoparticles, the oriented growth process of the stems occurred from the agglomerated particles. The small stems grew oriented around a single common center, forming a microparticle in the CaVO-4 sample (Figure 4a). The increase in the synthesis time to 8 min (CaVO-8 sample) favored an elongation of the stems, joined with a length of 6 μm and width of 644 nm, and their stem ends appeared faceted. Thus, the morphology is similar to a straw bundle with two fantails of stems, which are connected to each other in the middle (Figure 4b). During the synthesis, the effect of the

DOI: 10.1021/acs.inorgchem.8b02807
Inorg. Chem. XXXX, XXX, XXX−XXX

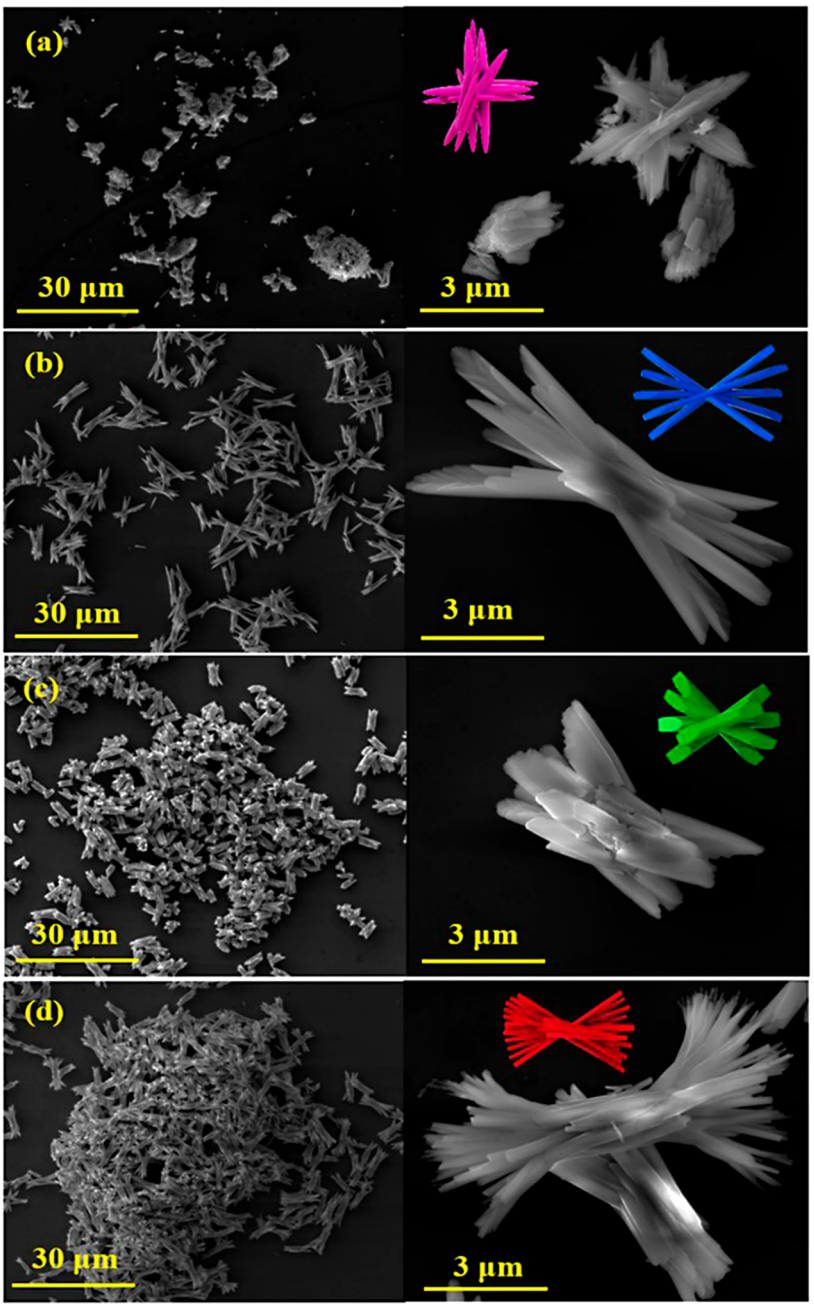

Figure 4. Low (30 μm) and high (3 μm) magnification FE-SEM images of the $Ca_{10}V_6O_{25}$ crystals processed at 120 °C as a function of synthesis time: (a) 4 min, (b) 8 min, (c) 16 min, and (d) 32 min. Inset illustrates the morphology of the crystals in pink, blue, green, and red.

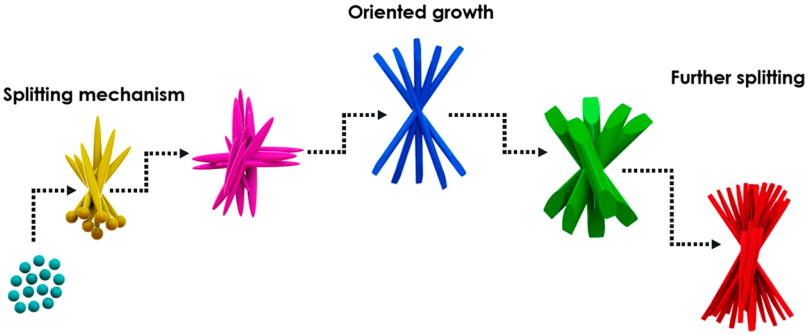

Figure 5. Growth mechanism of the $Ca_{10}V_6O_{25}$ crystal as a function of synthesis time: 4 min (pink), 8 min (blue), 16 min (green), and 32 min (red).

DOI: 10.1021/acs.inorgchem.8b02807
Inorg. Chem. XXXX, XXX, XXX−XXX

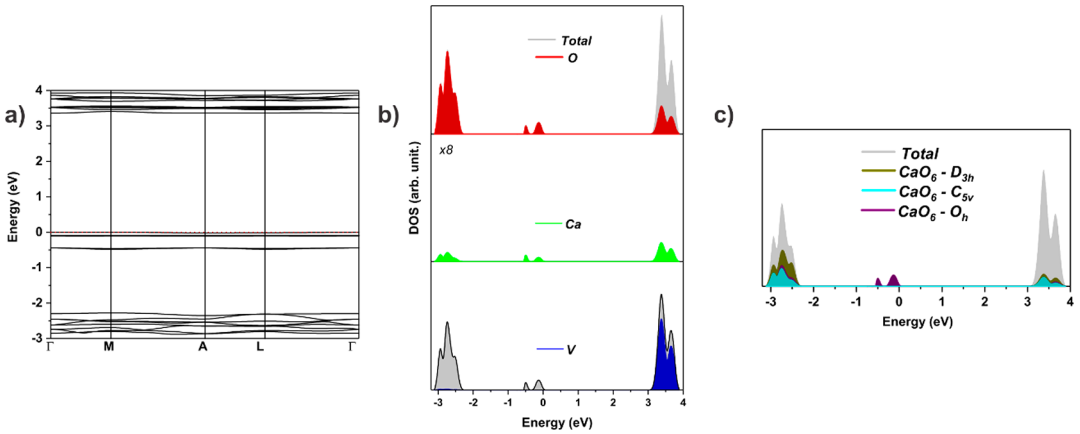

Figure 6. (a) Band structure, (b) total and atom-resolved DOS, and (c) Ca-centered cluster resolved DOS for $Ca_{10}V_6O_{25}$ material. In both cases, the Fermi level was set to zero.

microwaves on the particles caused a contraction of the stems (time of 16 min), which were aggregated, generating an increase of 1.1 μm in the width and a decrease of 2.6 μm in the length of the CaVO-16 sample (Figure 4c). It can be observed that, for a synthesis time of 16 min, there was a significant reduction of isolated rods in the sample. Further increasing the synthesis time to 32 min provoked the dissolution and recrystallization processes, with a concomitant elongation of the rods (Figure 4d). These rods were split into nanofilaments during the growth process, forming a particle with more ramifications. The CaVO-32 crystal presented tubes with the length of 6.67 μm and smaller width (230 nm) than the crystals obtained within a shorter synthesis time.

The growth process of the $Ca_{10}V_6O_{25}$ particles can be considered to be a crystal splitting mechanism. The nanocrystals are developed in large crystals, and these are divided to form stems, which are subdivided into nanofilaments as a bundle of straw shape. The division of the crystal is related to the rapid kinetics of crystal growth, supersaturation of the solution, and surface energy.[56−59] Figure 5 shows a series of morphologies formed according to the growth time of the $Ca_{10}V_6O_{25}$ particles. Thus, we observe that a single crystal is subdivided by means of a single nucleus. Along with the growth of the particle, there is a change in the $[CaO_6]$ clusters, and thus, different morphologies that are dependent on the synthesis time and the presence of microwaves are observed.

It can be observed that the MAH method allowed us to obtain materials with good structural ordering at short time and low temperature (120 °C at 4 min) with well-defined morphology. The interaction of the microwave energy with the particles or ions accelerates the diffusion mechanism, allowing the collision with other ions, atoms, or neighboring molecules, generating heat and thus reducing sintering time and temperature.[23] These shocks are fast and effective, which cause small distortions in bond length and angles in the $[CaO_6]$ and $[VO_4]$ clusters of the crystal lattice. Thus, with the increase of the synthesis time, the microwaves cause a restructurization of the clusters forming order and disorder locally, which can be seen as medium-range by the modification in the orientations of the clusters. These distortions in clusters generate defects as quantum dots, which favor the different PL properties of the material.

4.4. Optical Properties. *4.4.1. UV-vis Diffused Reflectance.* The optical properties of the $Ca_{10}V_6O_{25}$ semiconductors prepared at different times (4, 8, 16, and 32 min) at 120 °C via the MAH method were investigated using UV-vis and PL emissions at room temperature. $Ca_{10}V_6O_{25}$ has a direct-type optical transition.[10] According to the Wood−Tauc function,[60] $\alpha h\nu = C_1(h\nu - E_{gap})^n$, where $n = {}^1/_2$, α is the absorption coefficient, $h\nu$ is the photon energy, C_1 is a proportionality constant, and n is the type of electronic transition. Thus, we have $(\alpha h\nu)^2$, which can be related to the Kubelka−Munk function (K−M),[61] and we obtain the band-gap energy (E_{gap}) values of the samples using the graph $[F(R)h\nu]^2$ vs $h\nu$ (Figure S3 in the Supporting Information), where $F(R)$ is the K−M function.

UV-vis spectra show that all the samples of $Ca_{10}V_6O_{25}$ absorbed energy in the ultraviolet. An analysis of the results renders that the samples present an E_{gap} values at 4.04, 4.04, 3.94, and 3.84 eV at CaVO-4, CaVO-8, CaVO-16, and CaVO-32, respectively (see Figure S3). According to the Wood−Tauc function, a crystalline and ordered material has a well-defined absorption (vertical black dashed curve), and, therefore, for the $Ca_{10}V_6O_{25}$ crystal, a band gap (E_{gap}) of 4.3 eV is expected. Moreover, it can be observed that the variation in the synthesis time did not change the E_{gap} values of the $Ca_{10}V_6O_{25}$ samples. However, a slope of the optical absorption curves can be observed, indicating the presence of medium-range defects, which decreased the E_{gap} of the samples. The medium-range distortion on the $[CaO_6]_d$ and $[VO_4]_d$ clusters leads to a nonzero difference in the formal load between the clusters, thus causing a polarization in the system. The medium-range polarization generates an orientation interaction, since it causes the rotation motion of the permanent moments in different $[CaO_6]-[CaO_6]$, $[VO_4]-[VO_4]$, or $[CaO_6]-[VO_4]$ clusters. These interactions produce localized electronic levels within the forbidden band gap, which cause the entrapment of electrons and holes. Thus, the intrinsic PL emissions can be associated with these mechanisms, which are derived from the interactions between distorted clusters. In this way, the coupling of the vibrational and rotational movements modifying the intrinsic properties generating new materials. These properties are related to the defect densities, that is, order−disorder of the crystals.

To clarify the electronic structure of $Ca_{10}V_6O_{25}$, total and atom-resolved density of states (DOS) and band structures profiles were obtained, and the corresponding results are presented in Figure 6. In the left panel (Figure 6a), the band structure profile for $Ca_{10}V_6O_{25}$ is presented, in the middle panel (Figure 6b), the total and atom-resolved DOS curves are presented, whereas in the right panel (Figure 6c), a cluster-resolved DOS curve is depicted focusing on the contribution of

DOI: 10.1021/acs.inorgchem.8b02807
Inorg. Chem. XXXX, XXX, XXX−XXX

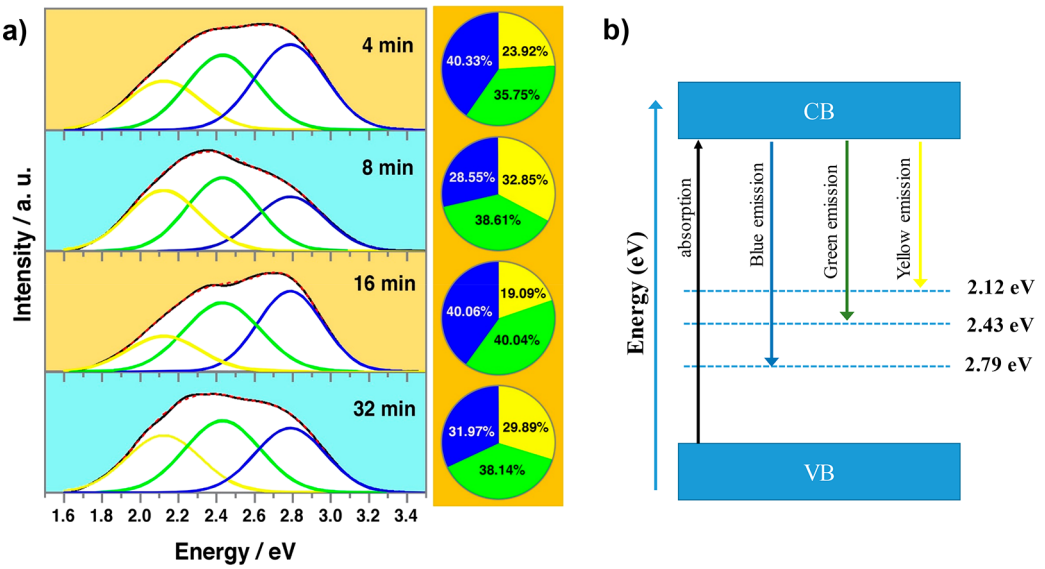

Figure 7. (a) Photoluminescence spectra at room temperature (black line), deconvolution (red dashed), and percentage of color area, blue (444 nm, 2.79 eV), green (510 nm, 2.43 eV), and yellow (585 nm, 2.12 eV), of the $Ca_{10}V_6O_{25}$ processed at 120 °C as a function of synthesis time. (b) Schematic representation of the PL emissions associated with the presence of the intermediated levels between the conduction band (CB) and the valence band (VB).

different $[CaO_6]$ clusters with singular symmetries. An analysis of the both valence and conduction bands (VB and CB, respectively) show a pattern, which is directly associated with the local clusters centered on Ca and V cations. The VB was predominantly composed of the orbitals of oxygen anions with a small content of Ca orbitals. In contrast, the CB was mostly based on empty valence orbitals from V cations hybridized with oxygen atomic orbitals, revealing the role of $[VO_4]$ clusters.

Let us now briefly discuss the relationship between the local coordination of both V and Ca cations and the electronic structure of the $Ca_{10}V_6O_{25}$ crystal. The optimized crystalline structure obtained for $Ca_{10}V_6O_{25}$ indicates that Ca cations have a 6-fold coordination $[CaO_6]$ with distinct local environments, as presented in Figure 2. Despite the same coordination number, the local arrangement indicates the formation of distorted octahedral, prism, and pentagonal-pyramidal symmetries. These distorted polyhedral symmetries provoke a local disorder along the crystalline structure, which perturbs the energy level distribution in the VB. From the energy levels distribution depicted in Figure 6c, it can be observed that the VB region exhibits two intermediate levels of energy, which can be directly related to the local geometries associated with Ca-centered clusters. Indeed, the first contribution located between −3.15 eV and −2.28 eV is related to the presence of all Ca-centered clusters with a major contribution of approximately prismatic $[CaO_6]$ clusters. In addition, it was noted that, at the vicinity of the Fermi level (between −0.46 eV and 0.0 eV), the electronic states are related to the distorted Ca-centered octahedral clusters. Therefore, the distortion associated with the crystalline structure of the $Ca_{10}V_6O_{25}$ results in a singular energy-level distribution that controls its electronic properties.

In addition, the obtained band structure profiles indicate that both VB maxima and CB minimum regions present flat energy bands against the symmetry points, resulting in a small difference between the direct and indirect band gap values, which helps achieve superior electrical and optical properties. The calculated band gap is 3.35 eV; in contrast, the experimental value reported here is 4.04 eV. This difference can be associated with almost two factors, as follows: (i) the as-synthesized $Ca_{10}V_6O_{25}$ materials exhibits a high degree of structural disorders with the presence of intermediary energy levels at the forbidden region, and (ii) the theoretical values are computed by using the hybrid B3LYP functional and their drawbacks to obtain accurate values of the band gap are well-known.[62,63]

Hojamberdiev and co-workers[10] successfully used hydrothermal methods to grow $Ca_{10}V_6O_{25}$ crystals, which showed a semiconducting behavior with band-gap values of ∼3.7 eV, which is consistent with our theoretical and experimental data. In this case, it can be assumed that the electron transfer associated with the band-gap value involves the excitation of VBM electrons, which are located at the orbitals linked to the Ca−O bonds of the highly distorted octahedral $[CaO_6]$ clusters, to orbitals or empty states located at the V−O bond of the $[VO_4]$ clusters.

4.4.2. PL Emissions. Figure 7 shows the PL spectra at room temperature, with the wavelength of excitation of 350 nm. All of the samples had a broadband profile covering the entire visible region of light. The PL spectra were deconvoluted to understand the behavior of the PL property of the $Ca_{10}V_6O_{25}$ samples. The Voigt Area G/L function was used, and three components were centered in the yellow (2.12 eV, 585 nm), green (2.43 eV, 510 nm) and blue (2.79 eV, 444 nm) regions.

It can be observed that the CaVO-4 and CaVO-16 samples have a higher percentage of emission in the blue and green regions, whereas, for the CaVO-8 and CaVO-32 samples, a higher percentage of emission in the yellow region is observed, which is related to the presence of the intrinsic structural defects of the samples. These defects generate intermediated levels between VB and CB. Therefore, the fast growth process and formation of smaller stems causes a high concentration of defects associated with structural distortions in the $[VO_4]$ clusters. An analysis of the deconvolution of PL emissions displayed in Figure 7a renders that emission energy in the yellow region corresponds to 2.12 eV, being lower than the energies in

DOI: 10.1021/acs.inorgchem.8b02807
Inorg. Chem. XXXX, XXX, XXX−XXX

the blue region (2.79 eV, and green, 2.43 eV, regions (see Figure 7b).

Both dissolution and recrystallization processes during the synthesis favor the formation of elongated stems in these samples, generating oxygen vacancies and surface defects. Three different charge states of oxygen vacancies may occur: the $[VO_3.V_0^x]$ state, which presents two paired electrons and is neutral in relation to the lattice; the singly ionized $[VO_3.V_0^{\cdot}]$ state, which has one unpaired electron; the $[VO_3.V_0^{\cdot\cdot}]$ state, which is doubly positively charged, with respect to the lattice. It is believed that these different types of structural defects that are generated by medium-range distortion that give rise to PL at room temperature. Since, the distortion causes the polarization in the structure and enable the formation of localized states in the band gap, as well as the inhomogeneous charge distribution in the cell, allowing the entrapment of electrons. The distribution of the localized levels allows various energies to be able to excite the trapped electrons. Broadband PL emission for all $Ca_{10}V_6O_{25}$ samples (Figure 7) shows the participation of numerous energy levels within the band gap, where the shift observed in the maximum emission point is due to variations on the density of structural defects.

A PL mechanism for disordered solids has been very reported in the literature and first-principles calculations are very important to elucidate such a mechanism.[46,47,64] In such mechanism structural defects, the creation of oxygen vacancies from the disorder of clusters, as the building block of the material is responsible for the formation of excited singlet (s*) and triplet (t*) electronic states related to PL phenomena. In particular, for our $Ca_{10}V_6O_{25}$ samples synthesized at various times, the experimental results show a similar response; thus, structural defects are important to investigate this material. Oxygen vacancies are the strongest evidence of the structural and electronic disorder in $[CaO_6]$ clusters; high concentration of disorder in clusters results in excited electronic states. Therefore, we proceed to the localization and characterization of the excited electronic states of the $Ca_{10}V_6O_{25}$ system.

4.4.2.1. Excited States. Figure S4 in the Supporting Information, shows the 3D optimized structure of the excited states, singlet (s*) and triplet (t*), and the local structures of the constituent clusters, which are compared with the fundamental structure of the fundamental singlet electronic state (see Figure 2). First, we note that the obtained geometries for s* and t* exhibit imaginary frequencies (see Table S3 in the Supporting Information). The singlet excited electronic state, s*, as the ground state (Table S2) corresponds to a saddle point (−79.33 cm^{-1}) on a very flat potential energy surface, whereas the excited triplet electronic state, t*, exhibits a very high and negative imaginary frequency (−1966.99 cm^{-1}), showing large structural instability. All attempts to adjust the geometries and eliminate these negative values were unsuccessful.

An analysis of Figure S4 shows that three different local arrangements with singular symmetries (D_{3h}, C_{5v}, and O_h) were observed for both s* and t*. The DOS and band structure profiles obtained for the fundamental and excited states are depicted in Figure S5 in the Supporting Information. Regarding the calculated band-gap value for s*, a similar value (3.29 eV) to the electronic ground-state was observed, as the VB is mainly composed of O (2p) states and the CB is predominantly formed by the V (3d) atomic state (Figure S5a in the Supporting Information). The main differences were attributed to the band degeneration in the s* state (Figure S5a), which can be attributed to the displacement of V atoms in the $[VO_4]$ cluster. In addition, the calculated band structure for the t* state (Figure S5b) indicates a band-gap value of 1.35 eV, which is a reduced value, in comparison with the singlet ground state. This electron transfer mechanism was described as a charge transfer from the 2p orbitals of disordered octahedral $[CaO_6]$ clusters to the 3d orbitals of $[VO_4]$ clusters (Figure S5b), indicating that the unpaired electron density generated in the t* state is located in the 3d empty orbitals of V atoms. The electron transfer from VB to CB perturbs the electron density distribution along the $[CaO_6]$ clusters, reordering the charge in the crystalline structure once the uppermost contributions of VB related to the presence of distorted octahedral clusters become high in energy, relative to the molecular orbitals of prismatic and pyramidal clusters.

Therefore, this wideband model enables the observation of the electronic features associated with the transformation from a fundamental s state to excited s* and t* states. In the CB, the t* state induces the creation of intermediary energy levels near the band-gap region responsible for the trapping of excited electrons. The calculated results confirm the electron transfer mechanism predicted from the DOS and band structure profiles (Figure 6). Notably, the unpaired density is mainly located on the $[VO_4]$ clusters closer to the highly distorted $[CaO_6]$ octahedra. The high distortion of $[CaO_6]$ clusters causes an increase in VBM, featuring the electronic excitation process as a charge transfer from $[CaO_6]$ clusters to $[VO_4]$ clusters. Therefore, the PL process is understood in the first moment as an excitation from the fundamental state (s) to an excited energy state (t*), which possesses a relative energy of 3.41 eV, in comparison with the ground state. The subsequent step can be described as an intersystem crossing process from the excited t* state to an s* electronic state, which exhibits a lower relative energy (1.03 eV), compared with the fundamental state. Once this excited s* electronic state is sufficiently populated, the PL emission occurs with a concomitant return to a ground electronic state.

The transformations from fundamental s (Figure 2) to both excited s* and t* electronic states (Figure S4), at prismatic (D_{3h}) and pyramidal (C_{5v}) clusters, are accompanied by a local disorder for both short and long Ca−O bonds, showing a general shortening of the chemical bonds. In contrast, the octahedral (O_h: centered in Ca5−7) cluster shows a bond expansion from the fundamental s state to the excited s* state, whereas the transformation from s* to t* is accompanied by a bond contraction. Regarding the structural disorders associated with the tetrahedral $[VO_4]$ cluster, it was observed that the transformation from s to s* involves the off-center displacement of V atoms in the *z*-direction, resulting in an in-plane bond elongation and out-of-plane bond contraction. This local disorder also affects the other V atoms in the crystalline structure exhibiting distorted V−O bonds. Furthermore, the transformation from s* to t* suggests a higher local disorder for $[VO_4]$ clusters, where the V−O bond length increases.

A careful inspection of the obtained values indicates that the transformation from the fundamental s state to the excited s* and t* states is predominantly attributed to the symmetrical stretching vibration of the V−O bond associated with the mode described by four degenerated frequencies: 859.60 cm^{-1} in the fundamental state and 854.88 cm^{-1} in the s* state, which becomes nondegenerated for the t* state, which exhibits frequencies of 531.25 and 830.70 cm^{-1}, consistent with the structural disorders summarized in Figure S4. This suggests a transition to a lower symmetry without bond breaking, which

DOI: 10.1021/acs.inorgchem.8b02807
Inorg. Chem. XXXX, XXX, XXX−XXX

involves the structural order−disorder effect originating from the off-centering V displacement, modifying not only the V−O bond lengths, but also the interaction among the electronic distributions of the atoms of the cell.

4.5. Measurements of Current versus Voltage. Figure 8 shows the current−voltage (I−V) characterization of the

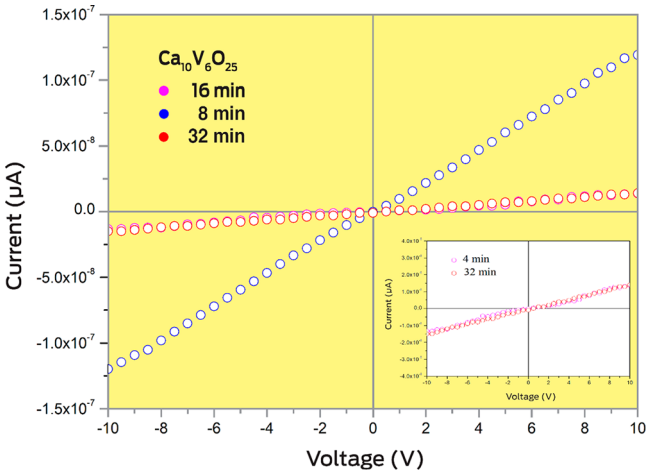

Figure 8. Current−voltage for the $Ca_{10}V_6O_{25}$ samples (with time 4, 8, and 32 min in 120 °C by MAH) at room temperature.

$Ca_{10}V_6O_{25}$ samples. The curves showed that the electric current in the samples presented a linear dependence with the voltage, showing an ohmic character at room temperature. It can be observed that the CaVO-4 and CaVO-32 samples showed lower electrical conductivity, compared with the CaVO-8 sample. This is possibly due to the trapping of electrons, which would be free to conduct; one reason for this behavior is the presence of oxygen molecules adsorbed on the surface or to the electron−hole recombination process. The CaVO-8 sample exhibited a greater conductivity than the other samples, and thus, it has a greater availability of free electrons. The CaVO-8 sample has numerous vanadium−oxygen vacancy centers, because of a higher percentage of emission in the yellow and red regions (see Figure 7). Oxygen vacancies form positive charges in the $Ca_{10}V_6O_{25}$ crystal lattice, favoring the diffusion of electrons when an external voltage is applied. Thus, a large current was observed in the CaVO-8 sample. However, for the CaVO-16 sample, a very high resistance was observed and the conductivity was not measured (Figure S6 in the Supporting Information). From the PL spectrum, it was observed that this sample has a higher emission in the blue and green regions, which are directly related to the intrinsic structural defects. These defects trap electrons, increasing the resistivity of the material. Moreover, in this sample, the interconversion of octahedral clusters to prismatic and pyramidal clusters of calcium may have occurred. These prismatic and pyramidal clusters show a tendency to form materials with resistivity character. In addition, the morphology of the CaVO-16 sample may have favored these more-resistive calcium clusters.

From the theoretical point of view, the electrical properties of the $Ca_{10}V_6O_{25}$ crystal can be understood using the symmetry-adapted molecular orbitals depicted in Figure 6, where the VB is described by two different oxygen contributions, because of the existence of several $[CaO_6]$ clusters. Therefore, the existence of conductive behavior of the samples can be attributed to the presence of highly distorted octahedral clusters contributing to the upper part of VB, whereas the resistive response is related to the pyramidal and prismatic clusters that contribute to the inner VB region.

However, all the samples exhibited low conduction, which is a characteristic of semiconductor materials. It can be observed that the synthesis time influenced the ordering of the material and the transport properties of electrons.

5. CONCLUSIONS

A facile, fast, and environmentally friendly method was reported for the synthesis of $Ca_{10}V_6O_{25}$ crystals. This new structure was prepared via the MAH method, which favors the growth of crystals with different morphologies through time variation. The XRD and Raman patterns showed a complex structure with $P6_3/m$ space group symmetry, formed by distorted $[VO_4]$ with various distorted $[CaO_6]$ clusters. Well-faceted and highly crystalline microcrystals were observed, consistent with the XRD and theoretical and experimental Raman spectroscopic analysis. The degree of short organization of the Ca clusters is a determinant of PL emissions. The charge transfer process between $[VO_4]$ and $[CaO_6]$ clusters is responsible for the presence of the singlet and triplet excited electronic states. In addition, the strong influence of defects (intrinsic structural defects and oxygen vacancy) on the electron diffusion in the samples can be observed. The sample that exhibited a greater percentage of oxygen vacancies favored the electron transport. Furthermore, depending on the synthesis conditions used for obtaining these crystals, different morphologies and distortions in their lattice, mainly associated with the distortions of the $[VO_4]$ and $[CaO_6]$ clusters, can be observed, and thus, they can exhibit different electronic properties. These results summarize the relevant contributions to the understanding of the structural, electronic, and optical properties of $Ca_{10}V_6O_{25}$ crystals and the growth mechanism involved during the MAH processing.

■ ASSOCIATED CONTENT

Supporting Information

The Supporting Information is available free of charge on the ACS Publications website at DOI: 10.1021/acs.inorgchem.8b02807.

Rietveld refinements and DFT calculations for $Ca_{10}V_6O_{25}$ material; Raman frequencies calculated B3LYP frequencies (ω) of the Raman active modes at the Γ point for the $P6_3/m$ structure; Raman frequencies calculated for $Ca_{10}V_5O_{25}$ crystal in the singlet (s*) and triplet (t*) excited state; full width at half-maximum of the peak of 352 cm^{-1} in the Raman spectra of all the $Ca_{10}V_5O_{25}$ samples; UV-vis diffuse reflectance spectra for $Ca_{10}V_6O_{25}$ samples; schematic representation of the constituent clusters; total and atom-resolved DOS and bands structures profiles at s* and t* electronic states; current−voltage characterizations for the $Ca_{10}V_6O_{25}$ crystal at 16 min in 120 °C by MAH at room temperature (DOC)

Accession Codes

CCDC 1851953−1851956 contain the supplementary crystallographic data for this paper. These data can be obtained free of charge via www.ccdc.cam.ac.uk/data_request/cif, or by emailing data_request@ccdc.cam.ac.uk, or by contacting The Cambridge Crystallographic Data Centre, 12 Union Road, Cambridge CB2 1EZ, UK; fax: +44 1223 336033.

DOI: 10.1021/acs.inorgchem.8b02807
Inorg. Chem. XXXX, XXX, XXX−XXX

AUTHOR INFORMATION

Corresponding Author

*E-mail: mayaramondego.ufma@gmail.com.

ORCID

Mayara Mondego Teixeira: 0000-0001-9038-0024
Regiane Cristina de Oliveira: 0000-0002-7332-8731
Renan Augusto Pontes Ribeiro: 0000-0002-4128-8296
Sergio R. de Lazaro: 0000-0001-9753-7936
Juan Andrés: 0000-0003-0232-3957
Elson Longo: 0000-0001-8062-7791

Notes

The authors declare no competing financial interest.

ACKNOWLEDGMENTS

This study was financed in part by the Coordenação de Aperfeiçoamento de Pessoal de Nível Superior - Brasil (CAPES) - Finance Code 001 and financial support of agencies: FAPESP (2013/07296-2; 2013/26671-9), CNPq (304531/2013-8), Generalitat Valenciana for PrometeoII/2014/022, Prometeo/2016/079, ACOMP/2014/270, ACOMP/2015/1202, Ministerio de Economia y Competitividad, project CTQ2015-65207-P, Universitat Jaume I for project UJI-B2016-25, Programa de Cooperación Cientifica con Iberoamerica (Brasil) of Ministerio de Educació (PHBP14-00020). M.C. acknowledges Generalitat Valenciana for Santiago Grisolia Program 2015/033. R.R. and S.R.L. thanks the UEPG, CAPES and Fundação Araucaria for the financial support. We thank Prof. Enio Longo for the images. The authors also thank the Servei d'Informàtica, Universitat Jaume I, for generous allocation of computer time.

REFERENCES

(1) Jouanneau, S.; Verbaere, A.; Guyomard, D. On a new calcium vanadate: synthesis, structure and Li insertion behavior. *J. Solid State Chem.* **2003**, *172* (1), 116−122.

(2) Luke, G. M.; Fudamoto, Y.; Gingras, M. J. P.; Kojima, K. M.; Larkin, M.; Merrin, J.; Nachumi, B.; Uemura, Y. J. Spin freezing and ordering in CaV_4O_9, CaV_3O_7 and CaV_2O_5. *J. Magn. Magn. Mater.* **1998**, *177*−*181*, 754−755.

(3) Parhi, P.; Upreti, S.; Ramanan, A. Crystallization of Calcium Vanadate Solids from Solution: A Metathetic Route. *Cryst. Growth Des.* **2010**, *10* (12), 5078−5084.

(4) Falcón, H.; Alonso, J. A.; Casais, M. T.; Martínez-Lope, M. J.; Sánchez-Benítez, J. Neutron diffraction study, magnetism and magnetotransport of stoichiometric $CaVO_3$ perovskite with positive magnetoresistance. *J. Solid State Chem.* **2004**, *177* (9), 3099−3104.

(5) Li, L.; Zheng, S.; Wang, S.; Du, H.; Zhang, Y. Thermal hydrolysis synthesis and characterization of monoclinic metahewettite $CaV_6O_{16}\cdot 3H_2O$. *J. Wuhan Univ. Technol., Mater. Sci. Ed.* **2014**, *29* (3), 433−440.

(6) Curelaru, I. M.; Strid, K. G.; Suoninen, E.; Minni, E.; Rönnhult, T. Electron structure of excited configurations in $Ca_2V_2O_7$ studied by electron-induced core-ionization loss spectroscopy, appearance-potential spectroscopy, and x-ray-photoelectron spectroscopy. *Phys. Rev. B: Condens. Matter Mater. Phys.* **1981**, *23* (8), 3700−3709.

(7) Parhi, P.; Manivannan, V.; Kohli, S.; McCurdy, P. Synthesis and characterization of $M_3V_2O_8$ (M = Ca, Sr and Ba) by a solid-state metathesis approach. *Bull. Mater. Sci.* **2008**, *31*, 885−890.

(8) Tong, Y. P.; Luo, G. T.; Jin, Z.; Lin, Y. W. Synthesis, Structure, and Theoretical Investigations of an Alkaline Earth Vanadate Oxide Compound ($Ca_4V_4O_{14}$): Electronic, Optical, and Chemical Bond Properties. *Aust. J. Chem.* **2011**, *64*, 973−977.

(9) Jacob, K. T.; Gupta, P. Gibbs energy of formation of $Ca_7V_4O_{17}$. *J. Chem. Thermodyn.* **2013**, *63*, 7−10.

(10) Hojamberdiev, M.; Bozgeyik, M. S.; Abdullah, A. M.; Bekheet, M. F.; Zhu, G.; Yan, Y.; Xu, Y.; Okada, K. Hydrothermal-induced growth of $Ca_{10}V_6O_{25}$ crystals with various morphologies in a strong basic medium at different temperatures. *Mater. Res. Bull.* **2013**, *48* (4), 1388−1396.

(11) Pei, L.; Pei, Y.; Xie, Y.; Fan, C.; Li, D.; Zhang, Q. Formation process of calcium vanadate nanorods and their electrochemical sensing properties. *J. Mater. Res.* **2012**, *27* (18), 2391−2400.

(12) Nakajima, T.; Isobe, M.; Tsuchiya, T.; Ueda, Y.; Manabe, T. Correlation between Luminescence Quantum Efficiency and Structural Properties of Vanadate Phosphors with Chained, Dimerized, and Isolated VO_4 Tetrahedra. *J. Phys. Chem. C* **2010**, *114*, 5160−5167.

(13) Pei, L. Z.; Pei, Y. Q.; Xie, Y. K.; Yuan, C. Z.; Li, D. K.; Zhang, Q.-F. Growth of calcium vanadate nanorods. *CrystEngComm* **2012**, *14* (13), 4262.

(14) Zhang, S.; Mu, W. Fabrication of $Ca_2V_2O_7$ microspheres and its application in lithium-ion batteries. *Mater. Lett.* **2016**, *183*, 311−314.

(15) Ogo, S.; Onda, A.; Yanagisawa, K. Hydrothermal synthesis of vanadate-substituted hydroxyapatites, and catalytic properties for conversion of 2-propanol. *Appl. Catal., A* **2008**, *348* (1), 129−134.

(16) Qiu, K.; Li, J.; Li, J.; Lu, X.; Gong, Y.; Li, J. Luminescence property of $Ca_3(VO_4)_2$:Eu^{3+} dependence on molar ratio of Ca/V and solution combustion synthesis temperature. *J. Mater. Sci.* **2010**, *45* (20), 5456−5462.

(17) Zhan, G.; Ng, W. C.; Koh, S. N.; Wang, C.-H. Template-Free Synthesis of Alkaline Earth Vanadates Nanomaterials from Leaching Solutions of Oil Refinery Waste. *ACS Sustainable Chem. Eng.* **2018**, *6* (2), 2292−230.

(18) Li, L.; Wang, S.; Du, H.; Zheng, S.; Zhang, Y. Equilibrium Data of the $KOH-K_3VO_4-Ca(OH)_2-H_2O$ System at (313.2 and 353.2) K. *J. Chem. Eng. Data* **2012**, *57* (9), 2367−2372.

(19) Adams, D. M.; Gardner, I. R. Single-crystal Vibrational Spectra of Apatite, Vanadinite, and Mimetite. *J. Chem. Soc., Dalton Trans.* **1974**, *14*, 1505−1509.

(20) Petit, S.; Gode, T.; Thomas, C.; Dzwigaj, S.; Millot, Y.; Brouri, D.; Krafft, J. M.; Rousse, G.; Laberty-Robert, C.; Costentin, G. Incorporation of vanadium into the framework of hydroxyapatites: importance of the vanadium content and pH conditions during the precipitation step. *Phys. Chem. Chem. Phys.* **2017**, *19* (14), 9630−9640.

(21) Frost, R. L.; Crane, M.; Williams, P. A.; Theo Kloprogge, J. Isomorphic substitution in vanadinite $[Pb_5(VO_4)_3Cl]$- a Raman spectroscopic study. *J. Raman Spectrosc.* **2003**, *34* (3), 214−220.

(22) Bartholomäi, G.; Klee, W. E. The vibrational spectra of pyromorphite, vanadinite and mimetite. *Spectrochim. Acta, Part A* **1978**, *34*, 831−843.

(23) Baghbanzadeh, M.; Carbone, L.; Cozzoli, P. D.; Kappe, C. O. Microwave-assisted synthesis of colloidal inorganic nanocrystals. *Angew. Chem., Int. Ed.* **2011**, *50* (48), 11312−59.

(24) Komarneni, S.; Roy, R.; Li, Q. H. Microwave-hydrothermal synthesis of ceramic powders. *Mater. Res. Bull.* **1992**, *27*, 1393−1405.

(25) Bilecka, I.; Niederberger, M. Microwave chemistry for inorganic nanomaterials synthesis. *Nanoscale* **2010**, *2* (8), 1358.

(26) Oliver Kappe, C. Microwave dielectric heating in synthetic organic chemistry. *Chem. Soc. Rev.* **2008**, *37* (6), 1127.

(27) Moreira, M. L.; Andrés, J.; varela, J. A.; Longo, E. Synthesis of Fine Micro-sized $BaZrO_3$ Powders Based on a Decaoctahedron Shape by the Microwave-Assisted Hydrothermal Method. *Cryst. Growth Des.* **2009**, *9*, 833−839.

(28) Volanti, D. P.; Sato, A. G.; Orlandi, M. O.; Bueno, J. M. C.; Longo, E.; Andrés, J. Insight into Copper-Based Catalysts: Microwave-Assisted Morphosynthesis, In Situ Reduction Studies, and Dehydrogenation of Ethanol. *ChemCatChem* **2011**, *3*, 839−843.

(29) da Silva, L. F.; Avansi, W.; Andres, J.; Ribeiro, C.; Moreira, M. L.; Longo, E.; Mastelaro, V. R. Long-range and short-range structures of cube-like shape $SrTiO_3$ powders: microwave-assisted hydrothermal synthesis and photocatalytic activity. *Phys. Chem. Chem. Phys.* **2013**, *15* (29), 12386−93.

(30) da Silva, L. F.; Catto, A. C.; Avansi, W.; Cavalcante, L. S.; Mastelaro, V. R.; Andrés, J.; Aguir, K.; Longo, E. Acetone gas sensor based on α-Ag_2WO_4 nanorods obtained via a microwave-assisted hydrothermal route. *J. Alloys Compd.* **2016**, *683*, 186−190.

DOI: 10.1021/acs.inorgchem.8b02807
Inorg. Chem. XXXX, XXX, XXX−XXX

(31) Dovesi, R.; Orlando, R.; Erba, A.; Zicovich-Wilson, C. M.; Civalleri, B.; Casassa, S.; Maschio, L.; Ferrabone, M.; De La Pierre, M.; D'Arco, P.; Noel, Y.; Causa, M.; Rerat, M.; Kirtman, B. CRYSTAL14: A Program for the Ab Initio Investigation of Crystalline Solids. *Int. J. Quantum Chem.* **2014**, *114*, 1287−1317.
(32) Becke, A. D. Density-functional thermochemistry. III. The role of exact exchange. *J. Chem. Phys.* **1993**, *98* (7), 5648−5652.
(33) Lee, C.; Yang, W.; Parr, R. G. Development of the Colle-Salvetti correlation-energy formula into a functional of the electron density. *Phys. Rev. B: Condens. Matter Mater. Phys.* **1988**, *37* (2), 785−789.
(34) Beltrán, A.; Gracia, L.; Andrés, J.; Longo, E. First-Principles Study on Polymorphs of $AgVO_3$: Assessing to Structural Stabilities and Pressure-Induced Transitions. *J. Phys. Chem. C* **2017**, *121* (49), 27624−27642.
(35) Oliveira, M. C.; Gracia, L.; de Assis, M.; Rosa, I. L. V.; do Carmo Gurgel, M. F.; Longo, E.; Andrés, J. Mechanism of photoluminescence in intrinsically disordered $CaZrO_3$ crystals: First principles modeling of the excited electronic states. *J. Alloys Compd.* **2017**, *722*, 981−995.
(36) Ribeiro, R. A. P.; de Lazaro, S. R.; Pianaro, S. A. Density Functional Theory applied to magnetic materials: Mn_3O_4 at different hybrid functionals. *J. Magn. Magn. Mater.* **2015**, *391*, 166−171.
(37) Moreira, M. L.; Buzolin, P. G.; Longo, V. M.; Nicoleti, N. H.; Sambrano, J. R.; Li, M. S.; Varela, J. A.; Longo, E. Joint experimental and theoretical analysis of order-disorder effects in cubic $BaZrO_3$ assembled nanoparticles under decaoctahedral shape. *J. Phys. Chem. A* **2011**, *115* (17), 4482−90.
(38) Oliveira, F. K. F.; Oliveira, M. C.; Gracia, L.; Tranquilin, R. L.; Paskocimas, C. A.; Motta, F. V.; Longo, E.; Andrés, J.; Bomio, M. R. D. Experimental and theoretical study to explain the morphology of $CaMoO_4$ crystals. *J. Phys. Chem. Solids* **2018**, *114*, 141−152.
(39) Valenzano, L.; Torres, F. J.; Doll, K.; Pascale, F.; Zicovich-Wilson, C. M.; Dovesi, R. Ab Initio Study of the Vibrational Spectrum and Related Properties of Crystalline Compounds; the Case of $CaCO_3$ Calcite. *Z. Phys. Chem.* **2006**, *220*, 893−912.
(40) Mackrodt, W. C.; Harrison, N. M.; Saunders, V. R.; Allan, N. L.; Towler, M. D.; Aprà, E.; Dovesi, R. Ab initio Hartree-Fock calculations of CaO, VO, MnO and NiO. *Philos. Mag. A* **1993**, *68* (4), 653−666.
(41) Corno, M.; Busco, C.; Civalleri, B.; Ugliengo, P. Periodic ab initio study of structural and vibrational features of hexagonal hydroxyapatite $Ca_{10}(PO_4)_6(OH)_2$. *Phys. Chem. Chem. Phys.* **2006**, *8* (21), 2464−72.
(42) Monkhorst, H. J.; Pack, J. D. Special points for Brillouin-zone integrations. *Phys. Rev. B* **1976**, *13* (12), 5188−5192.
(43) da Silva, L. F.; M'Peko, J.-C.; Andrés, J.; Beltrán, A.; Gracia, L.; Bernardi, M. I. B.; Mesquita, A.; Antonelli, E.; Moreira, M. L.; Mastelaro, V. R. Insight into the Effects of Fe Addition on the Local Structure and Electronic Properties of $SrTiO_3$. *J. Phys. Chem. C* **2014**, *118* (9), 4930−4940.
(44) Moreira, M. L.; Buzolin, P. G. C.; Longo, V. M.; Nicoleti, N. H.; Sambrano, J. R.; Li, M. S.; Varela, J. A.; Longo, E. Joint Experimental and Theoretical Analysis of Order−Disorder Effects in Cubic $BaZrO_3$ Assembled Nanoparticles under Decaoctahedral Shape. *J. Phys. Chem. A* **2011**, *115* (17), 4482−4490.
(45) Longo, V. M.; das Graca Sampaio Costa, M.; Zirpole Simoes, A.; Rosa, I. L. V.; Santos, C. O. P.; Andres, J.; Longo, E.; Varela, J. A. On the photoluminescence behavior of samarium-doped strontium titanate nanostructures under UV light. A structural and electronic understanding. *Phys. Chem. Chem. Phys.* **2010**, *12* (27), 7566−7579.
(46) Gracia, L.; Longo, V. M.; Cavalcante, L. S.; Beltrán, A.; Avansi, W.; Li, M. S.; Mastelaro, V. R.; Varela, J. A.; Longo, E.; Andrés, J. Presence of excited electronic state in $CaWO_4$ crystals provoked by a tetrahedral distortion: An experimental and theoretical investigation. *J. Appl. Phys.* **2011**, *110* (4), 043501.
(47) Gracia, L.; Andrés, J.; Longo, V. M.; Varela, J. A.; Longo, E. A theoretical study on the photoluminescence of $SrTiO_3$. *Chem. Phys. Lett.* **2010**, *493* (1−3), 141−146.
(48) Oliveira, M. C.; Gracia, L.; de Assis, M.; Rosa, I. L. V.; do Carmo Gurgel, M. F.; Longo, E.; Andrés, J. Mechanism of photoluminescence in intrinsically disordered $CaZrO_3$ crystals: First principles modeling of the excited electronic states. *J. Alloys Compd.* **2017**, *722*, 981−995.
(49) Rietveld, H. M. Line profiles of neutron powder-diffraction peaks for structure refinement. *Acta Crystallogr.* **1967**, *22*, 151.
(50) Larson, A. C.; Von Dreele, R. B. *General Structure Analysis System (GSAS)*; Technical Report, Los Alamos National Laboratory: Los Alamos, NM, 2001; pp 124−213.
(51) Wilhelmi, K. A.; Jonsson, O.; Karvonen, P.; Kjær, A.; Shapiro, R. H.; Westerdahl, A. X-Ray Studies on Some Alkali and Alkaline-Earth Chromates (V). *Acta Chem. Scand.* **1965**, *19*, 177−184.
(52) Momma, K.; Izumi, F. VESTA: a three-dimensional visualization system for electronic and structural analysis. *J. Appl. Crystallogr.* **2008**, *41* (3), 653−658.
(53) Momma, K.; Izumi, F. VESTA 3for three-dimensional visualization of crystal, volumetric and morphology data. *J. Appl. Crystallogr.* **2011**, *44* (6), 1272−1276.
(54) Longo, V. M.; Cavalcante, L. S.; Paris, E. C.; Sczancoski, J. C.; Pizani, P. S.; Li, M. S.; Andrés, J.; Longo, E.; Varela, J. A. Hierarchical Assembly of $CaMoO_4$ Nano-Octahedrons and Their Photoluminescence Properties. *J. Phys. Chem. C* **2011**, *115* (13), 5207−5219.
(55) Moura, M. R.; Ayala, A. P.; Guedes, I.; Grimsditch, M.; Loong, C. K.; Boatner, L. A. Raman scattering study of $Tb(V_{1-x}P_x)O_4$ single crystals. *J. Appl. Phys.* **2004**, *95* (3), 1148−1151.
(56) Liu, K.; You, H.; Jia, G.; Zheng, Y.; Huang, Y.; Song, Y.; Yang, M.; Zhang, L.; Zhang, H. Hierarchically Nanostructured Coordination Polymer: Facile and Rapid Fabrication and Tunable Morphologies. *Cryst. Growth Des.* **2010**, *10* (2), 790−797.
(57) Tang, J.; Alivisatos, P. A. Crystal Splitting in the Growth of Bi_2S_3. *Nano Lett.* **2006**, *6*, 2701−2706.
(58) Zhao, Y.; Shi, H.; Chen, M.; Teng, F. Splitting growth of novel CuO straw sheaves and their improved photocatalytic activity due to exposed active {110} facets and crystallinity. *CrystEngComm* **2014**, *16* (12), 2417−2423.
(59) Wu, S.; Zhang, J.; Shi, L.; Tang, S.; Li, Y.; Jiang, L.; Cui, Q. Template-free synthesis of α-GaOOH hyperbranched nanoarchitectures via crystal splitting and their optical properties. *RSC Adv.* **2014**, *4* (16), 8209.
(60) Wood, D. L.; Tauc, J. Weak Absorption Tails in Amorphous Semiconductors. *Phys. Rev. B* **1972**, *5* (8), 3144−3151.
(61) Philips-Invernizzi, B. Bibliographical review for reflectance of diffusing media. *Opt. Eng.* **2001**, *40* (6), 1082.
(62) Franchini, C. Hybrid functionals applied to perovskites. *J. Phys.: Condens. Matter* **2014**, *26* (25), 253202.
(63) Garza, A. J.; Scuseria, G. E. Predicting Band Gaps with Hybrid Density Functionals. *J. Phys. Chem. Lett.* **2016**, *7* (20), 4165−4170.
(64) Moreira, M. L.; Andrés, J.; Gracia, L.; Beltrán, A.; Montoro, L. A.; Varela, J. A.; Longo, E. Quantum mechanical modeling of excited electronic states and their relationship to cathodoluminescence of $BaZrO_3$. *J. Appl. Phys.* **2013**, *114* (4), 043714.

DOI: 10.1021/acs.inorgchem.8b02807
Inorg. Chem. XXXX, XXX, XXX−XXX